Theoretical and experimental investigations of anchoring force loss behavior for prestressed ground anchors

Shimin Zhu [a,b], **Changfu Chen** [a,b], **Genbao Zhang**[c], and **Cheng Du**[a,b]

[a]Key Laboratory of Building Safety and Energy Efficiency of the Ministry of Education, Hunan University, Changsha, Hunan 410082, P.R. China; [b]College of Civil Engineering, Hunan University, Changsha, Hunan 410082, P.R. China; [c]College of Civil Engineering, Hunan City University, Yiyang, Hunan 413000, P.R. China

Corresponding author: **Changfu Chen** (email: cfchen@hnu.edu.cn)

Abstract

Anchoring force loss is critically concerned for the in-service performance of prestressed ground anchors. This time-dependent loss of pretension exerted at the anchor head is caused primarily by stress relaxation, which integrally manifests the rheological properties of the anchor and the geomaterial in which the anchor is embedded. A load-transfer modeling framework was established to derive the time-dependent anchoring force response. The modeling parameters were directly calibrated via element-scale pullout stress relaxation test using a specially developed setup. The applicability and effectiveness of this analytical modeling framework were verified via large-scale laboratory model tests and in situ tests of prestressed anchors. The predictions derived using the presented modeling framework were in good agreement with measurements in both laboratory model tests and in situ tests, particularly for evolutions of anchoring force over time. Sensitivity evaluation of the model parameters was performed to study their respective impact on the anchoring force loss response. This work can provide insights into the understanding of the anchoring force loss behavior of prestressed ground anchors and facilitate their design practice for in-service performance.

Key words: prestressed ground anchor, anchoring force loss, relaxation, load transfer

Résumé

La perte de la force d'ancrage est un problème critique pour la performance en service des ancrages de sol précontraints. Cette perte de la précontrainte exercée à la tête de l'ancrage, qui dépend du temps, est causée principalement par la relaxation des contraintes, qui se manifeste intégralement par les propriétés rhéologiques de l'ancrage et du géomatériau dans lequel il est encastré. Un cadre de modélisation du transfert de charge a été établi pour dériver la réponse de la force d'ancrage en fonction du temps. Les paramètres de modélisation ont été directement calibrés par un essai de relaxation de la contrainte d'arrachement à l'échelle de l'élément à l'aide d'une configuration spécialement développée. L'applicabilité et l'efficacité de ce cadre de modélisation analytique ont été vérifiées par des essais à grande échelle en laboratoire et des essais in situ sur des ancrages précontraints. Les prédictions obtenues à l'aide du cadre de modélisation présenté étaient en bon accord avec les mesures effectuées lors des essais sur modèle en laboratoire et des essais in situ, en particulier pour l'évolution de la force d'ancrage dans le temps. L'évaluation de la sensibilité des paramètres du modèle a été réalisée pour étudier leur impact respectif sur la réponse de la perte de la force d'ancrage. Ces travaux peuvent permettre de mieux comprendre le comportement de la perte de force d'ancrage des ancrages de sol précontraints et faciliter leur conception pour les performances en service. [Traduit par la Rédaction]

Mots-clés : ancrage de sol précontraint, perte de force d'ancrage, relaxation, transfert de charge

1. Introduction

Ground anchors have been widely adopted in various anchored geotechnical applications, such as dams, slopes, tunnels, and deep foundation pits, owing to their unique virtues of simple constructability, high strength, and economic benefits (Fang 1991; Zhang and Benmokrane 2005; Brown 2015; Ehrlich and Silva 2015; Štefaňák et al. 2017; Ozhan and Guler 2018; Shi et al. 2019; Bryson and Giraldo 2020; Zhu et al. 2021). A prestressed ground anchor is a kind of ground anchor belonging to an active supporting structure (Hobst and Zajic 1983; Li 2017). Reduction of pre-tension (anchoring force loss) is a highly concerning aspect for prestressed ground anchors in engineering practice (Li 2017; Chen et al. 2018; Shi et al. 2019). Additionally, the mechanical behaviors of this structure are time-dependent, characterized by the distributions of tensile force and shear stress varying with time

Can. Geotech. J. **59:** 1587–1601 (2022) | dx.doi.org/10.1139/cgj-2021-0220

1587

(Chen et al. 2021). Hence, it is of great importance to establish a new theoretical approach to describe the time-dependent mechanical behaviors of prestressed anchors; however, this is still not well studied in the reported works.

The anchoring force loss behavior of prestressed anchors is generally determined by the mechanical properties of the surrounding geomaterials and their own construction materials (e.g., rebar/stranded wire and cement grout) (Shi et al. 2019), and it can specifically be divided into the following aspects: factor (a), tension resilience of the anchorage device; factor (b), creep deformation of rebar and cement grout; factor (c), creep deformation of the surrounding soils/rocks; factor (d), interface creep behaviors between the grout and soil; and factor (e), the construction and environmental disturbance. Most researchers have adopted the anchor as an integrated element by assuming a consistent interface bond behavior over the entire bond length in previous studies. This holistic modeling method is typically characterized by incorporating and modifying classical rheological models (e.g., Kelvin model and Merchant model) to model the coupling effects of the abovementioned factors. For instance, Chen et al. (2018) have established a rheological model that can consider the coupling effects of factors (b) and (c); Shi et al. (2019) have established a rheological model that can consider the coupling effects of factors (a), (b), and (c). Additionally, Chen et al. (2016) and Zhang et al. (2020) studied the soil–grout interface shear creep behaviors by long-term pullout tests for element-scale grouted anchor specimens and further established interface shear creep models. Relaxation equations characterizing the anchoring force loss behavior were then deduced from these rheological models combined with initial conditions. However, it is noteworthy that the time-dependent distributions of tensile force and shear stress cannot be obtained according to this holistic modeling method. Additionally, ground anchors usually show varying mechanical properties over bond length, especially embedded in pan soil or rock (Farmer 1975). Therefore, this holistic modeling method may be roughly suitable for soft soil embedded due to the relatively uniform distribution of shear stress over the soil–grout interface but may have poor accuracy for pan soil or rock.

Previous studies on the load-transfer behaviors of grouted anchors have focused mainly on the working condition with short-term loads (Martín et al. 2011; Hong et al. 2012; Ma et al. 2013), that is, regardless of the time effect. The significance of these studies lies in revealing the distributions of tensile force over bond length, and obtaining the instantaneous ultimate bearing capacity. However, the reported studies relevant to the time-dependent load-transfer behaviors of anchors are still limited and focus mainly on non-prestressed ground anchors (Yang et al. 2014; Zhang et al. 2015; Chen et al. 2021). Some scholars have monitored the long-term anchoring force of prestressed anchors through in situ tests (Benmokrane and Ballivy 1991; Kim 2003; Chen et al. 2018) and laboratory model tests (Chen et al. 2002) and derived the anchoring force loss responses based on the measurements. However, most of them did not study the evolution of tensile force and shear stress over bond length with elapsed time.

The involvement of pretension makes the theoretical modeling of prestressed anchors differ from that of non-prestressed anchors in the following two aspects: (*i*) a higher order nonlinear partial differential equation is needed to characterize the load-transfer process by incorporating the rheological properties of the surrounding soil, anchor, and soil–grout interface, which is hard to explicitly formulate and solve, even using a simple rheological model, and (*ii*) the tensile force and pullout displacement at the tensioned end of the anchorage segment change with elapsed time due to the existence of the free segment and the rheological properties of materials and the soil–grout interface, which is in contrast to full-length grouted anchors and makes the modeling more difficult.

By incorporating the finite difference technique, a theoretical modeling framework was developed to derive the time-dependent mechanical behaviors, especially anchoring force loss, for prestressed ground anchors. The Merchant rheological model was adopted to characterize the interaction between grout and soil, and its parameters were directly calibrated via an element-scale pullout stress relaxation test. A large-scale laboratory model test for prestressed anchors embedded in laterite was conducted using a specially designed setup. The material properties and testing conditions of the element-scale pullout test were representative of those of the large-scale model test. The applicability and effectiveness of the presented theoretical modeling framework were verified by comparing the respective predictions of anchoring force loss derived in theoretical modeling with measurements in physical model tests and in situ tests. The evolutions of tensile force and interface shear stress over bond length were also discussed. Additionally, the impacts of different model parameters on the derived responses of anchoring force loss were investigated.

2. Theoretical modeling of prestressed ground anchors

2.1. Basic assumptions

To simplify the analysis procedures, the following assumptions were specially made in theoretical modeling:

1. The nonlinear soil properties can affect the interface creep behavior between the grout and soil due to the development of shear band (Zhang et al. 2020). The Merchant rheological model was adopted to characterize the interaction between the grout and surrounding soil because it excels other models by using fewer parameters to describe both creep and stress relaxation behaviors (Zhang et al. 2015). The creep behavior of the soil can also be considered in this model.

2. The failure of grouted anchors in practice is commonly characterized by interface debonding between the grout and soil due to the much lower interface bond strength than that between the grout and tension rod (Chu and Yin 2005). Hence, we took the tension rod and grout in the anchorage segment as a whole and further assumed that the tensile deformation of this whole is instantaneous

and elastic. The stress–strain response of the whole obeys Hooke's law.

3. For prestressed anchors, hot-rolled steel bars and steel strands are the most commonly used tension rods. In design practice, tension rods are generally equipped with a large strength safety reserve. In this case, the tensile strain of the tension rod in the free segment is small enough, and its creep effect can be nearly negligible. Hence, we assumed that the tension rod in the free segment is instantaneous and elastic, and its stress–strain response obeys Hooke's law.

4. Anchoring force loss caused by loose and rebound deformation of the anchorage device was neglected because it can generally be controlled by improving the method and quality of construction (Shi et al. 2019), so the pullout displacement at the anchor head was further assumed to be constant.

Based on the abovementioned assumptions, the time-dependent load-transfer behavior for prestressed anchors was analyzed as follows.

2.2. Governing equations

Figure 1 presents the analytical schematic of the time-dependent load-transfer behavior for prestressed anchors. The geometric equation, deformation equation, and force equilibrium equation of analytical modeling can all be reasoned from that.

Geometric equation: the relationship between the axial pullout displacement $s(x, t)$ and the axial strain $\varepsilon(x, t)$ of the grouted anchor can be expressed as

$$(1) \quad \varepsilon(x, t) = -\frac{\partial s(x, t)}{\partial x}$$

where x is the distance from the tensioned end in the anchorage segment and t is time.

Deformation equation: according to assumption (b), the axial strain of grouted anchor $\varepsilon(x, t)$ can be calculated

$$(2) \quad \varepsilon(x, t) = \frac{P(x, t)}{EA}$$

where $P(x, t)$ is the tensile force of the anchor, A represents the cross-sectional area of the anchorage segment, and E represents Young's modulus of the anchorage segment, which is a composite modulus of the tension rod and grout and can be calculated by eq. 3.

$$(3) \quad E = \frac{E_b A_b + E_g A_g}{A_b + A_g}$$

where E_b and E_g represent the elasticity modulus of the tension rod and grout, respectively, and A_b and A_g represent the cross-sectional area of the tension rod and grout, respectively.

Force equilibrium equation: for a separate segment of anchor with length dx, the force equilibrium equation can be expressed as

$$(4) \quad dP(x, t) + u_p \tau(x, t)\, dx = 0$$

where $\tau(x, t)$ is the soil–grout interface shear stress and μ_p is the perimeter of the anchor.

Equation 4 can be converted into the following form:

$$(5) \quad \frac{\partial P(x, t)}{\partial x} = -u_p \tau(x, t)$$

The Merchant rheological model is composed of a spring element and a Kelvin model in series, and its structure is presented in Fig. 1b. This model has only three parameters but is equipped with the capacity to describe both creep and stress relaxation behaviors and has been widely adopted in rheology studies of geotechnical materials (Zhang et al. 2015). The constitutive equation of the Merchant rheological model is

$$(6) \quad G_1 s(x, t) + \eta \frac{\partial s(x, t)}{\partial t} = \left(\frac{G_0 + G_1}{G_0}\right)\tau(x, t) + \frac{\eta}{G_0}\frac{\partial \tau(x, t)}{\partial t}$$

where G_0 and G_1 are the grout–soil interface shear moduli and η is the grout–soil interface shear viscosity coefficient.

The Merchant rheological model was adopted to simulate the interaction between the grout and the surrounding geomaterials. Combining eqs. 1, 2, and 5 with eq. 6, the governing equation can be deduced:

$$(7) \quad \frac{\partial g(x, t)}{\partial t} + b\frac{\partial^2 s}{\partial x^2} - cs = 0$$

$$(8) \quad g(x, t) = \frac{\partial^2 s}{\partial x^2} - as$$

where $a = \mu_p G_0/EA$, $b = (G_0 + G_1)/\eta$, and $c = \mu_p G_0 G_1/EA$.

Equation 7 is a third-order partial differential equation, and its closed-form solution is difficult to obtain. Hence, the finite difference method was used to solve this issue in the following.

2.3. Numerical solution

Prestressed anchors are usually loaded with designed pre-tensions in practice. According to assumption (d), the pullout displacement at the anchor head can be idealized as constant during the loading process, taking the designed pre-tension (initial anchoring force) as P_0 and assuming that the corresponding pullout displacement at the anchor head is constant, s_h. At the initial moment ($t = 0$), the distributions of tensile force, shear stress, and displacement along the bond length are derived as (refer to Appendix A for details)

$$(9) \quad \begin{cases} s(x, t_0) = \dfrac{P_0}{\beta EA(e^{2\beta L_a} - 1)}\left(e^{\beta x} + e^{2\beta L_a - \beta x}\right) \\[2mm] \tau(x, t_0) = \dfrac{G_0 P_0}{\beta EA(e^{2\beta L_a} - 1)}\left(e^{\beta x} + e^{2\beta L_a - \beta x}\right) \\[2mm] P(x, t_0) = \dfrac{P_0}{(e^{2\beta L_a} - 1)}\left(e^{2\beta L_a - \beta x} - e^{\beta x}\right) \end{cases}$$

where $\beta = \sqrt{\mu_p G_0/EA}$ and L_a is the length of the anchorage segment.

Equation 9 shows the initial conditions of the above governing equation (eq. 7). The pullout displacement at the ten-

Fig. 1. Analytical schematic of time-dependent load transfer behavior for prestressed ground anchors: (*a*) force analysis schematic and (*b*) structure of Merchant rheological model. [Color online.]
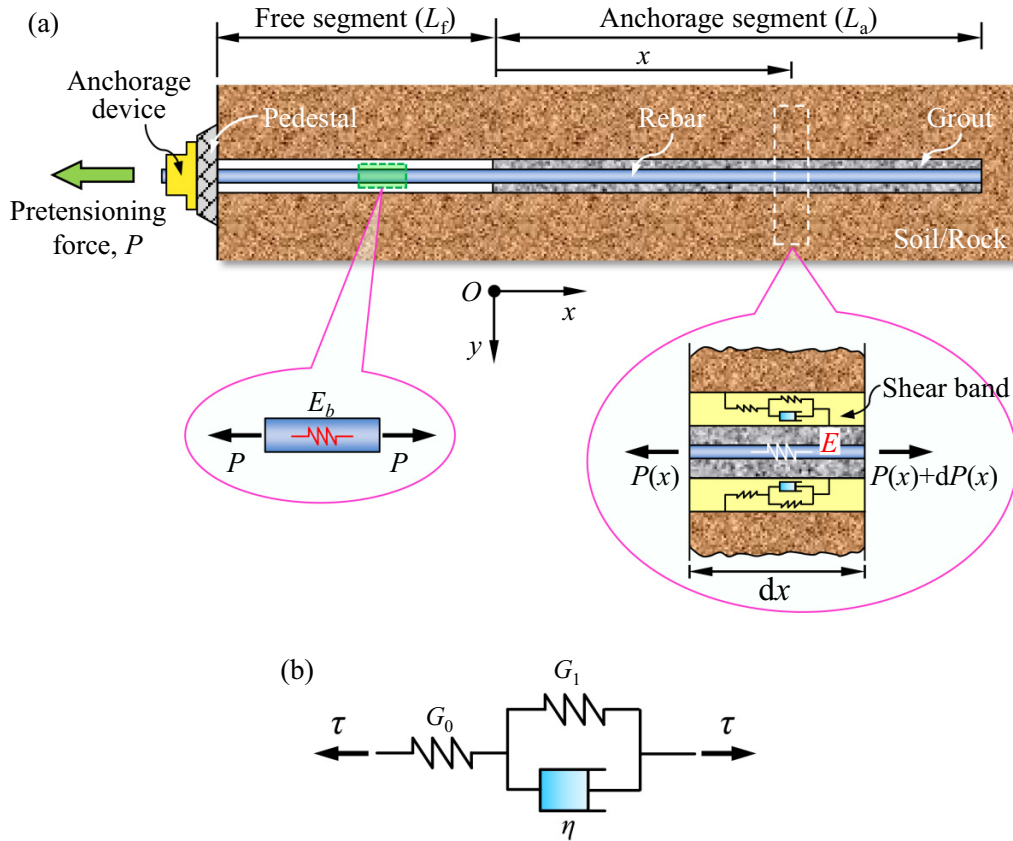
sioned end of the anchorage segment $s(x_0, t)$ changes with elapsed time. According to assumption (c), the relationship between $s(x_0, t)$ and s_h can be expressed as

$$(10) \quad s(x_0, t) = s_h - \delta_b(t) = s_h - \frac{P(x_0, t)}{E_b A_b} L_f$$

where L_f is the length of free segment and $\delta_b(t)$ is the tensile deformation of tension rod in free segment.

Further, combing with eqs. 9 and 10, the boundary conditions can be derived as

$$(11) \quad \begin{cases} \text{At anchor head:} \\ s_h = s_0(x_0, t_0) + \delta_b(t_0) = P_0 \left[\dfrac{(e^{2\beta L_a} + 1)}{\beta EA(e^{2\beta L_a} - 1)} + \dfrac{L_f}{E_b A_b} \right] \\ \text{At end of anchorage segment } (x = L_a): P = 0 \end{cases}$$

Equations 9 and 11 are the boundary value conditions for solving eq. 7. Figure 2 shows the programming flowchart for deriving the numerical solutions, which is presented in detail as follows.

Step 1 — The anchorage segment is discretized into n units along the axis with a uniform length of $\Delta x = L/n$ using $n + 1$ nodes. These nodes are numbered by 0, 1, 2, ..., n in sequence from the tensioned end to the free end. The value of n can be prescribed to meet the computational precision demand.

Fig. 2. Programing flowchart for deriving numerical solutions.
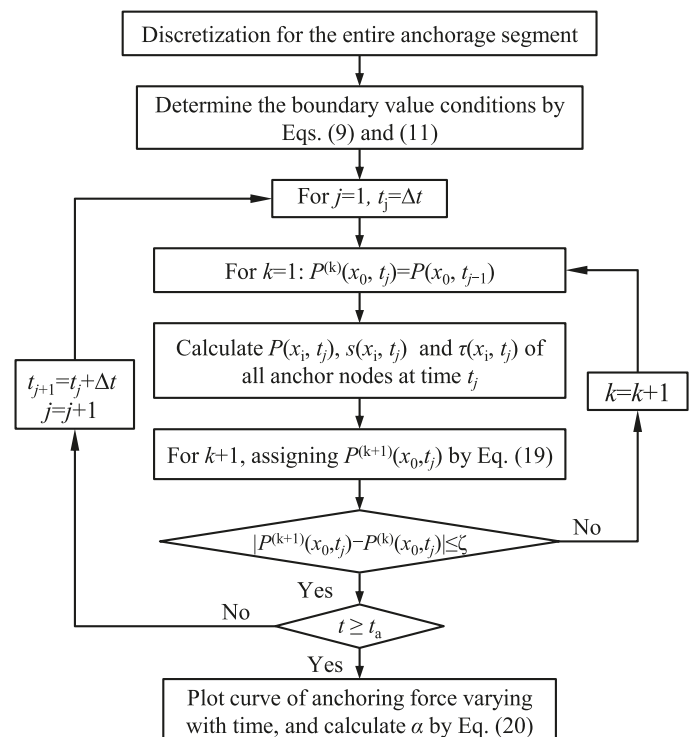
Step 2 — For $n-1$ internal nodes ($i = 1, 2, \ldots, n-1$), eq. 7 at arbitrary time t can be rewritten in the following finite difference form:

$$(12) \quad \frac{g(x_i, t + \Delta t) - g(x_i, t)}{\Delta t} + b\frac{\partial^2 s(x_i, t)}{\partial x^2} - cs(x_i, t) = 0$$
$$(i = 1, 2, \ldots, n-1)$$

where x_i represents the location of the ith node; Δt is the calculation step of time t that can be specified according to the computational precision demand.

Equation 12 can be rewritten as

$$(13) \quad g(x_i, t + \Delta t) = \left[cs(x_i, t) - b\frac{\partial^2 s(x_i, t)}{\partial x^2}\right]\Delta t + g(x_i, t)$$
$$(i = 1, 2, \ldots, n-1)$$

Step 3 — At the initial time t_0 ($t = 0$), $g(x, t_0)$ of all nodes is calculated to be zero by eqs. (8) and (9). $g(x_i, t_0 + \Delta t)$ can then be calculated by eq. 13.

Step 4 — For $n-1$ internal nodes ($i = 1, 2, \ldots, n-1$), establishing the difference scheme of eq. 8 for the location variable x

$$(14) \quad \frac{s(x_{i+1}, t_1) + s(x_{i-1}, t_1) - 2s(x_i, t_1)}{\Delta x^2} - as(x_i, t_1) = g(x_i, t_1)$$
$$(i = 1, 2, \ldots, n-1)$$

where t_1 is $t_0 + \Delta t$.

Equation 14 can be rewritten as

$$(15) \quad \frac{1}{\Delta x^2}s(x_{i+1}, t_1) - \frac{2+a}{\Delta x^2}s(x_i, t_1) + \frac{1}{\Delta x^2}s(x_{i-1}, t_1)$$
$$= g(x_i, t_1) \quad (i = 1, 2, \ldots, n-1)$$

The axial displacements $s(x_i, t_1)$ of all nodes at time $t_1 = t_0 + \Delta t$ are regarded as unknown quantities. Therefore, $n + 1$ equations are indispensably needed to solve these $n + 1$ unknown quantities. $g(x_i, t_1)$ of $n - 1$ internal nodes ($i = 1, 2, \ldots, n-1$) has been calculated in step 3, so $n - 1$ equations can be established as eq. 15.

Step 5 — For the other two nodes ($i = 0$ and n), combining with eqs. 1, 2, and 10, the corresponding two equations can be established as

$$(16) \quad \begin{cases} s(x_0, t_1) = s_h - \dfrac{P(x_0, t_1)}{E_bA_b}L_f \\ \dfrac{EA}{\Delta x}s(x_{n-1}, t_1) - \dfrac{EA}{\Delta x}s(x_n, t_1) = 0 \end{cases}$$

Notably, the tensile force at the tensioned end of the anchorage segment $P(x_0, t_1)$ is still unknown. Hence, the iterative method is also introduced. Specifically, taking $P^{(1)}(x_0, t_1) = P(x_0, t_0)$ in the first iterative computation, the superscript is the number of iterations. Combining eq. 15 with 16, a nonlinear equation set with $n + 1$ unknown quantities and $n + 1$ equations can thus be established. The axial displacement $s(x_i, t_1)$ of all the nodes at time $t_1 = t_0 + \Delta t$ can then be obtained by solving this equation set.

Step 6 — The tensile force and shear stress of all nodes at time t_1 can be calculated through eqs. 17 and 18, respectively.

$$(17) \quad P(x, t) = -EA\frac{\partial s(x, t)}{\partial x}$$

$$(18) \quad \tau(x, t) = \frac{EA}{\mu_p}\frac{\partial^2 s(x, t)}{\partial x^2}$$

Step 7 — For $k + 1$th iterative computation, taking

$$(19) \quad P^{(k+1)}(x_0, t_1) = \frac{\left[P(x_0, t_1) + P^{(k)}(x_0, t_1)\right]}{2}$$

Steps 5 through 7 are repeated until the values of $P(x_0, t_1)$ converge in subsequent iterations.

Step 8 — Steps 3 through 7 can be repeated to solve for the distributions of tensile force, shear stress, and axial displacement over the bond length at arbitrary times. The loss rate of the anchoring force α is usually defined as follows:

$$(20) \quad \alpha = \frac{P_0 - P(x_0, t_\infty)}{P_0}$$

where P_0 is the designed initial anchoring force and $P(x_0, t_\infty)$ is the stabilized anchoring force, which is approximate to the anchoring force at the anchor head when the calculation time t is relatively large.

By implementing the abovementioned procedures, a theoretical modeling framework of time-dependent mechanical behavior for prestressed anchors was established.

3. Element-scale pullout stress relaxation test for determining model parameters

The value of the model parameters is crucial for the theoretical simulation. An element-scale grouted anchor specimen was prepared, the bond length of which was limited to no more than four times the anchor diameter to ensure uniform distribution of the interface shear stress (Benmokrane et al. 1995; Zhang et al. 2020). The material properties and testing conditions of element-scale pullout tests are representative of those of anchors in the field. Therefore, element-scale pullout tests can be conducted to determine the interface bond–slip model parameters (Benmokrane et al. 1995; Ma et al. 2013; Chen et al. 2015). In this paper, an element-scale pullout stress relaxation test was specifically conducted to determine the Merchant model parameters that characterize the interaction between the soil and grout. It is noteworthy that the parameters obtained from the element-scale pullout test correspond to the large-scale model test in Section 4 and practically reflect the rheological properties of the soil–grout interface and the surrounding soils.

Table 1. Properties of the soil sample, tension rod, and cement grout.

Property	Value
Soil sample	
Natural water content, w (%)	33.6
Natural density, ρ (Mg/m^3)	1.64
Natural void ratio, e	1.21
Specific gravity, G_s	2.693
Liquid limit, w_l (%)	57.3
Plasticity limit, w_P (%)	33.9
Plasticity index, I_P (%)	23.4
Maximum dry density, ρ_{dmax} (g/cm^3)	1.58
Optimum water content, w_{opt} (%)	25.1
Cohesive force, c (kPa)	49.1
Internal friction angle, ϕ (°)	16.7
Modulus of compression, E_s (MPa)	2.77
Coefficient of uniformity, C_u	15
Coefficient of curvature, C_c	1.35
Tension rod	
Nominal diameter, d_n (mm)	16
Elasticity modulus, E_b (GPa)	210
Cement grout	
Type	P.O 42.5
Compressive strength, q_u (MPa)	30.5
Elasticity modulus, E_g (GPa)	13.5

3.1. Pullout stress relaxation test for element-scale grouted anchor specimen

The soil used was laterite under remolded conditions, the grouted material was cement paste with a water–cement ratio of 0.45, and the anchor body was ribbed steel rebar of 16 mm in diameter. The basic parameters of all the testing materials are summarized in Table 1.

The specimen was 300 mm in diameter, 80 mm in bond length, and 48 mm in anchor hole diameter. Generally, the influence zone of lateral friction resistance for a pile is between 5 and 10 times the pile diameter (Cook et al. 1979). Similar results were found for anchors via experimental investigation (Rajaie 1990; Chen et al. 2017). The diameter ratio between the specimen and the grout was 6.25, and it almost exceeded the influence zone of lateral friction resistance. Hence, the influence of the boundary effect could almost be eliminated. The ratio of the bond length (80 mm) to the diameter of the anchor hole (48 mm) was 1.67, which ensured a uniform distribution of shear stress over the bond length (Zhang et al. 2020). The moisture content and dry density of the specimen were 30% and 1.2 g/cm, respectively.

The procedures for preparing an element-scale anchor specimen include soil compaction, creation of an anchor hole, and grouting and curing, as shown in Fig. 3. After curing for 28 days, the prepared element-scale anchor specimen was assembled on a specially developed apparatus for pullout stress relaxation testing. The handle of the worm screw lifter was turned on to make the screw rod and the grout rise

slowly, and a pullout load was applied in the process. The handle was stopped when the pullout load reached a precalculated value (i.e., the simulated pretension). The pullout displacement at the anchor head was monitored to be constant during the loading period. The long-term variation of tensile force at the anchor head was monitored using a load cell and was further converted to the interface shear stress relaxation curve owing to the uniform stress distributions.

A multi-stage loading scheme was adopted in accordance with Tan and Kang (1980). Stress relaxation curves of n loading steps were obtained from only one specimen in this loading method, which is equivalent to n one-step loadings of various load levels on n different specimens. There were five loading steps with initial pullout loads P_0 of 120, 240, 360, 480, and 600 N, and the corresponding grout–soil interface shear stresses at the initial moment were almost 10, 20, 30, 40, and 50 kPa, respectively. Considering the long-term performance of the instruments, the loading time was set as 120 h (5 days) for each loading step. Figure 4 presents the time history curve of interface shear stress obtained during multi-stage pullout loading. For stress relaxation tests, the loading history under previous low stress levels does not influence the following test results under high stress levels. Hence, the time history curve under multi-stage loads was transformed into a cluster of stress relaxation curves corresponding to all five loading levels based on a coordinate transformation method, as shown in Fig. 5.

3.2. Determination of parameters in Merchant model

The Merchant rheological model (eq. 6) can be transformed into the following stress relaxation equation when the displacement/deformation remains constant.

$$(21) \quad \tau(t) = \tau_0 \left[\frac{G_1}{G_0 + G_1} + \frac{G_0}{G_0 + G_1} e^{\left(-\frac{G_0 + G_1}{\eta}t\right)} \right]$$

where τ_0 is the interface shear stress at the initial moment.

Equation 21 was used to fit the five interface shear stress relaxation curves, as shown in Fig. 5. Relationships between the three Merchant model parameters (G_0, G_1, and η) and the initial interface shear stress τ_0 were plotted in Fig. 6. G_0 and G_1 all decrease exponentially with increasing stress level, and η increases and then decreases, at least for the range of loading levels adopted in this test. In fact, it reflects the nonlinear mechanical behaviors of the soil–grout interface.

4. Large-scale model test of pretension loading on prestressed anchor

A large-scale physical model test of a prestressed anchor embedded in laterite was conducted to facilitate the verification of the presented theoretical modeling framework. It is particularly noteworthy that all the materials used in this large-scale model test were consistent with these used in the abovementioned element-scale pullout test, and their parameters are presented in Table 1. Long-term variations of the anchoring force at the anchor head and distributions of the ten-

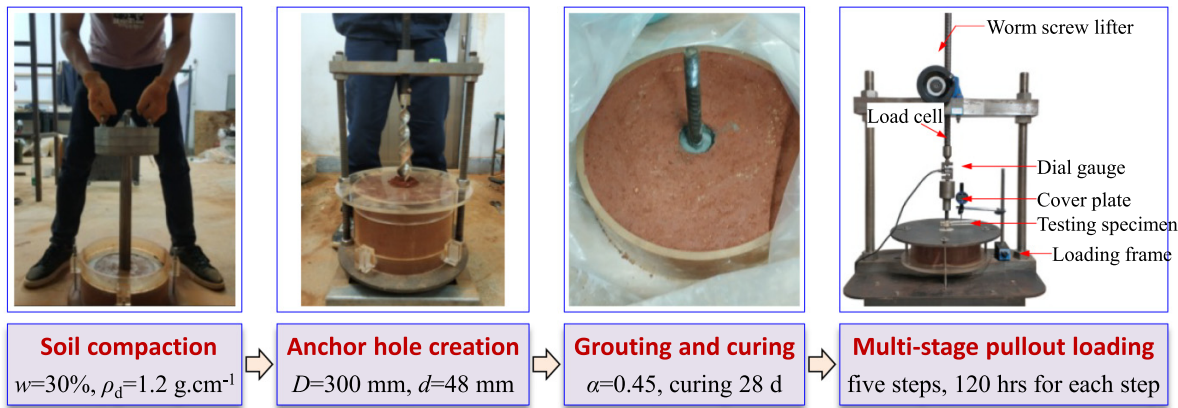**Fig. 3.** Programs of the element-scale pullout stress relaxation test. [Color online.]

Soil compaction	Anchor hole creation	Grouting and curing	Multi-stage pullout loading
w=30%, ρ_d=1.2 g.cm⁻¹	D=300 mm, d=48 mm	α=0.45, curing 28 d	five steps, 120 hrs for each step

Fig. 4. Time history curve of interface shear stress under multi-stage loads for the element-grouted anchor specimen. [Color online.]
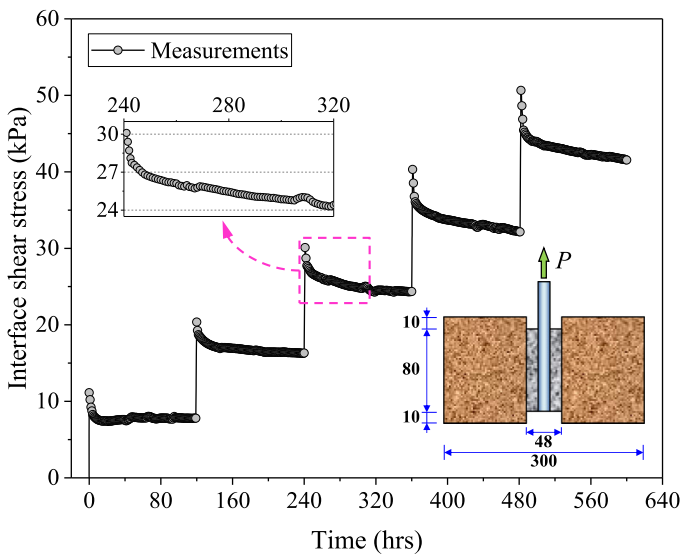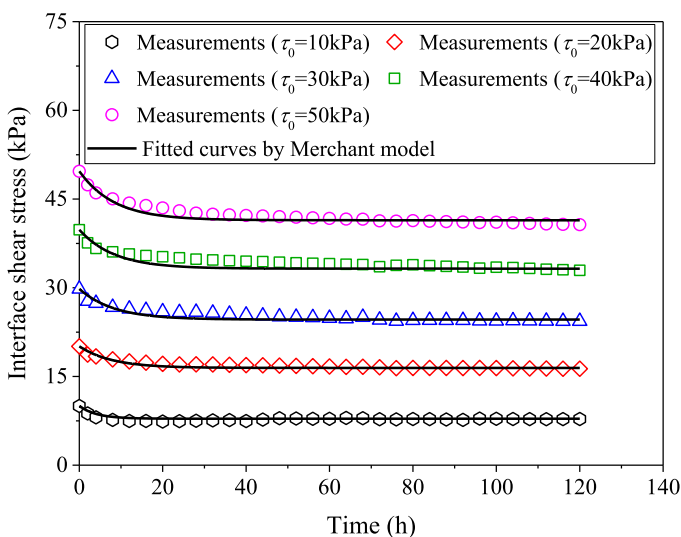

Fig. 5. Comparisons of the testing interface shear stress relaxation curves with the fitting results. [Color online.]

sile force were especially monitored. The setup, testing procedures, loading scheme, and results of the model test are discussed next.

4.1. Pullout setup and materials

The physical model specimen was 530 mm in diameter, 1500 mm in height, 1200 mm in bond length, 500 mm in free length, and 60 mm in anchor hole diameter, as shown in Fig. 7a. The ratio of the diameter of the specimen (530 mm) to the anchor hole diameter (60 mm) was 8.8. Similar to the element-scale pullout test, the influence of the boundary effect could almost be eliminated. Pullout loads were applied using a worm screw lifter equipped with greater capacity, as shown in Fig. 7. The anchoring force at the anchor head and the distribution of the tensile force over the bond length were monitored in real time using a load cell and eight pairs of strain gauges (with a DH3816 strain recorder), respectively.

4.2. Testing procedures and results

The procedures for preparing the large-scale prestressed anchor specimen were similar to those of preparing the element-scale grouted anchor specimen, including the following:

- *Assembling the specimen mold* — A steel tube covered with plastic film was preinstalled at the center of the specimen molds.
- *Soil compacting* — Remolded laterite with moisture content of 30% was filled into the acrylic tube and then compacted in layers with a dry density of 1.20 g/cm³.
- *Anchor hole creation* — Pulling out the preinstalled steel tube slowly after the laterite was compacted to the designed height (1500 mm). A uniform cylindrical hole with a diameter of 60 mm was then created at the center of the soil specimen to simulate the anchor hole.
- *Grouting* — The rebar plastered with eight pairs of strain gauges was installed at the center of the created hole, and then grouting with no pressure was conducted. Thereafter, the specimens were cured for 28 days in sealed condition.

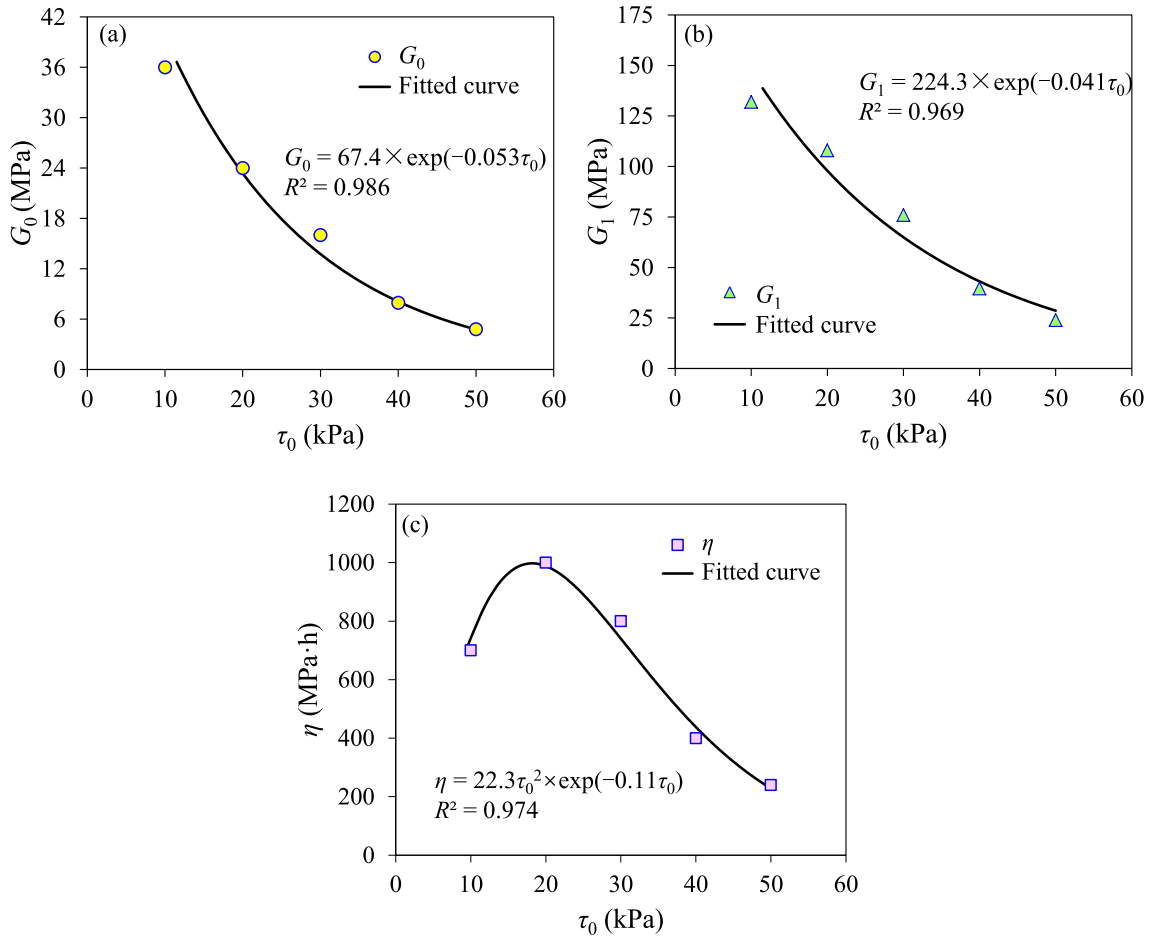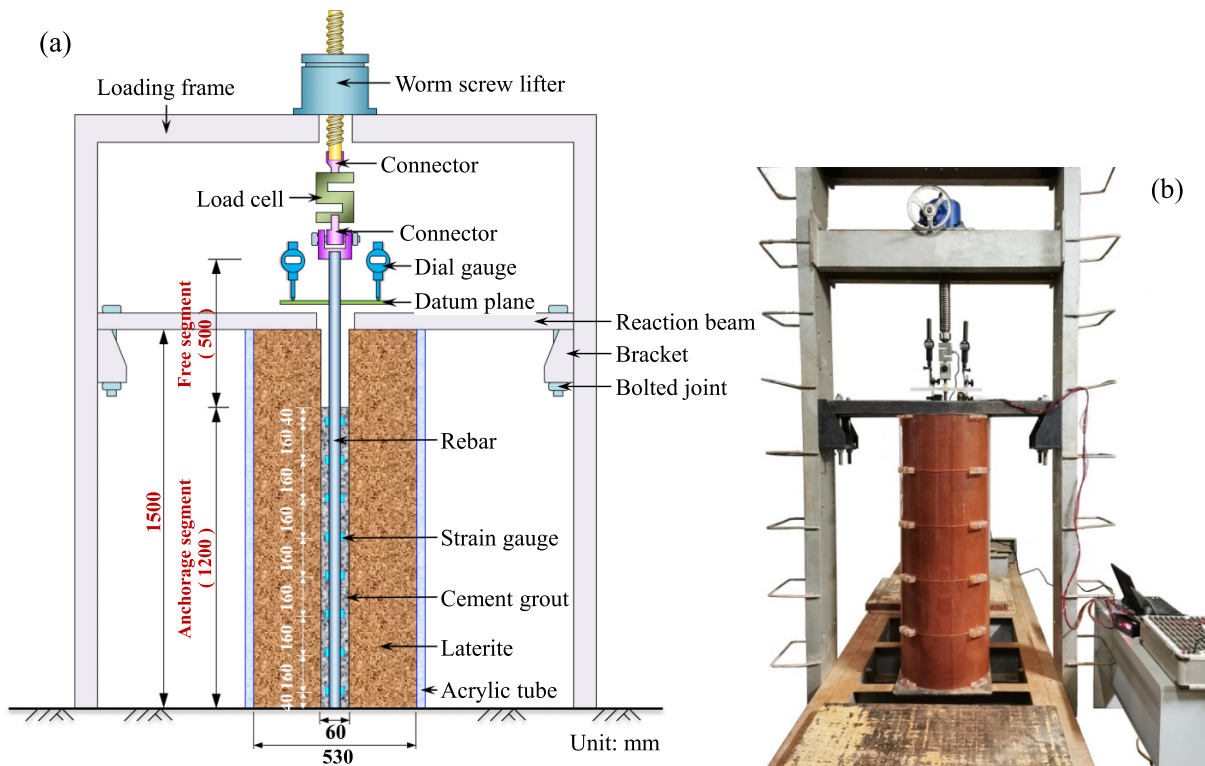**Fig. 6.** Merchant model parameters versus initial interface shear stress: (*a*) G_0; (*b*) G_1; and (*c*) η. [Color online.]

Fig. 7. Views of the pullout setup: (*a*) schematic illustration and (*b*) photograph. [Color online.]

Fig. 8. Time history curve of anchoring force at anchor head of large-scale anchor specimen under multi-stage pullout loads in model test. [Color online.]
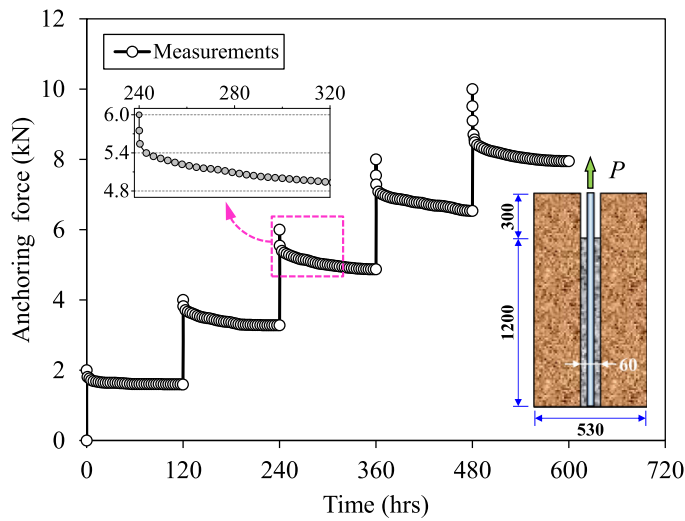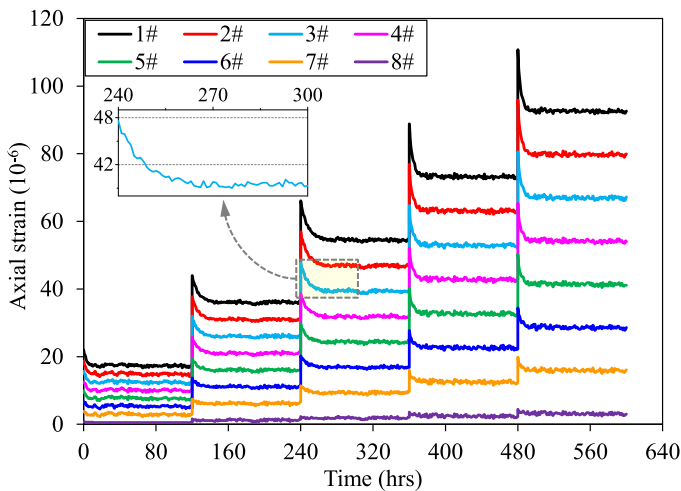

Fig. 9. Time history curves of axial strain for eight monitoring positions over bond length. [Color online.]

A multi-stage loading scheme was also adopted. The applied pullout loads were divided into five levels with the initial pretensions of 2.0, 4.0, 6.0, 8.0, and 10.0 kN. The time for each loading level was 120 h. Note that the initial interface shear stresses for the element-scale anchor specimen in the pullout stress relaxation test were consistently applied to the large-scale anchor specimen in the model test. Figure 8 presents the time history curve of the anchoring force at the anchor head obtained during the multi-stage pullout loading. Figure 9 shows the time history curves of axial strain for the eight monitoring positions over the bond length. Figure 8 was transformed into a cluster of anchoring force loss curves corresponding to all five loading levels, as shown in Fig. 10. The anchoring force was found to decrease with decay rate as time elapsed and finally tended to be stable. The loss rates of

Fig. 10. Predictions for five anchoring force loss curves of the physical model test using the presented analytical modeling framework. [Color online.]
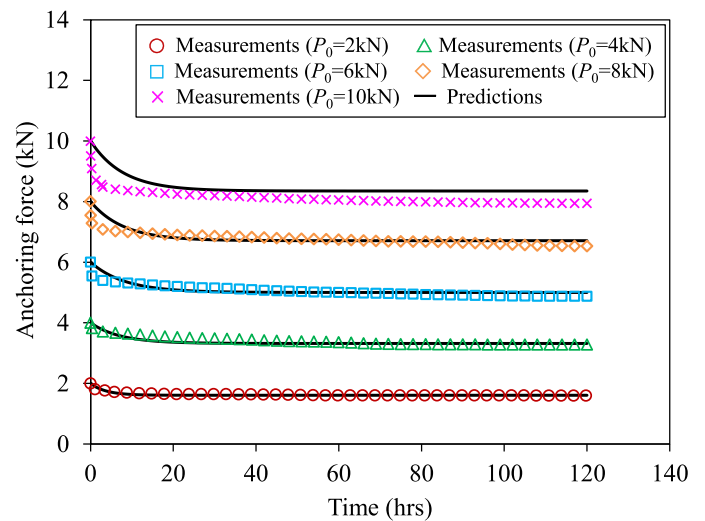

the anchoring force α were calculated as 20.3%, 18.1%, 18.8%, 18.3%, and 20.5% under the five loading levels.

4.3. Experimental verification for theoretical modeling

As mentioned above, the material properties and stress conditions for the element-scale anchor specimen were almost consistent with the large-scale model specimen. Therefore, model parameters obtained from the element-scale pullout test could be used in the experimental verification of the theoretical modeling. The model parameters obtained from the element-scale pullout test corresponding to the ith ($i = 1$, 2, …, 5) stress level were specifically used to predict the large-scale model testing results corresponding to the ith loading level to minimize the influence of the stress level. Predictions of anchoring force loss curves under five various load levels were derived using the theoretical modeling framework presented in Section 2, as shown in Fig. 10. Correlation coefficients R^2 and root mean square error (RMSE) indicated the good agreement between the predictions and measurements for the anchoring force loss curves: R^2 0.972 and RMSE 2.2% for $P_0 = 2$ kN; R^2 0.895 and RMSE 8.7% for $P_0 = 4$ kN; R^2 0.935 and RMSE 9.1% for $P_0 = 6$ kN; R^2 0.933 and RMSE 10.3% for $P_0 = 8$ kN; and R^2 0.959 and RMSE 14.2% for $P_0 = 10$ kN. Comparisons between predictions and measurements for distributions of tensile force and shear stress over bond length at different times are presented in Fig. 11. Both the tensile force and shear stress over the bond length decrease at a decay rate with time elapsed, and finally tend to be stable. The presented theoretical modeling framework has successfully captured this behavior, so it was confirmed to be able to characterize the time-dependent load-transfer behaviors for prestressed ground anchors. The tensile force is approximatively linear, and the interface shear stress is almost uniform over the bond length, which is due to the much greater stiffness of the anchor than the stiffness of the grout–soil interface.

Fig. 11. Predictions for distributions of tensile force and interface shear stress over bond length at different moments: (*a*) tensile force and (*b*) interface shear stress. [Color online.]
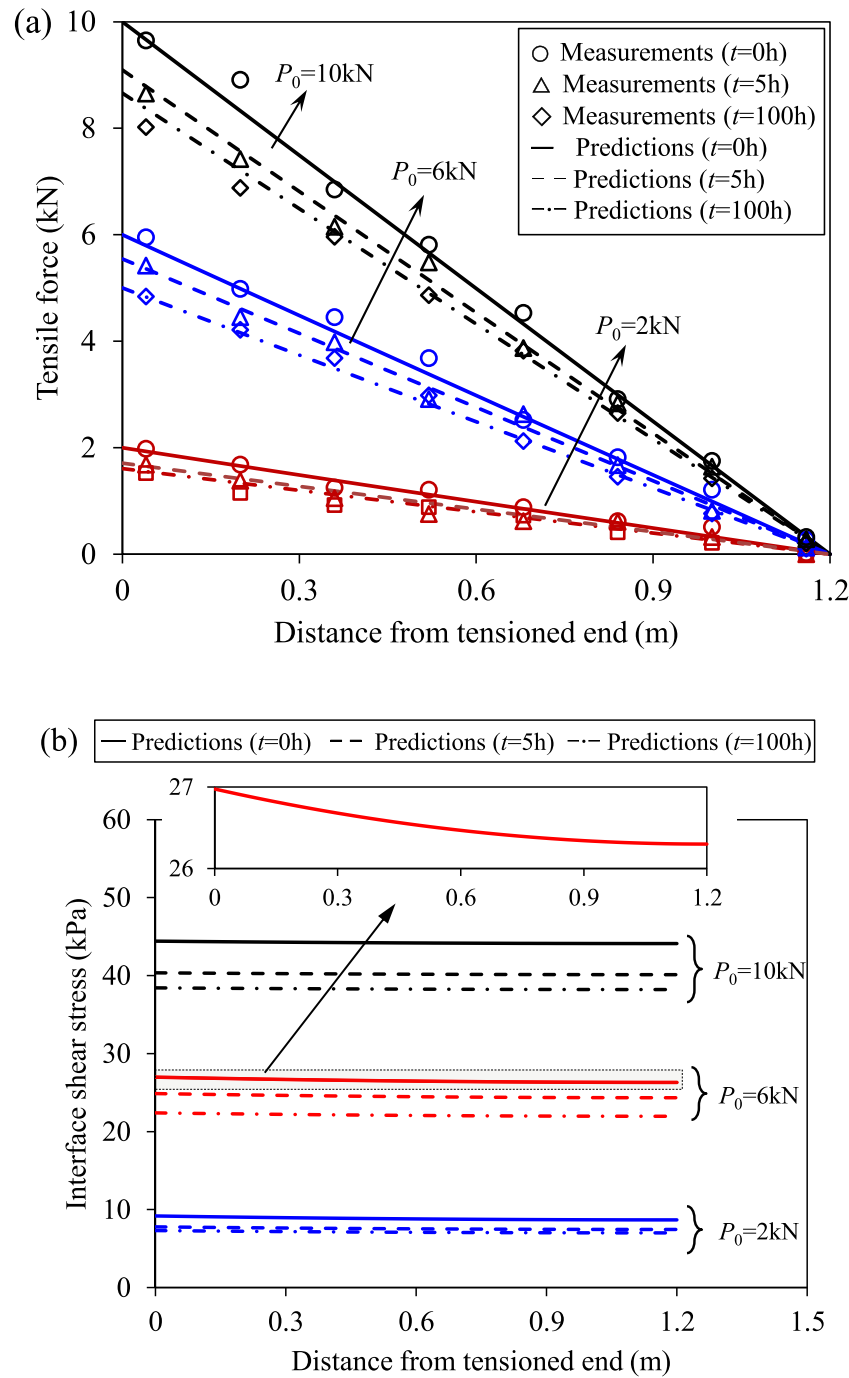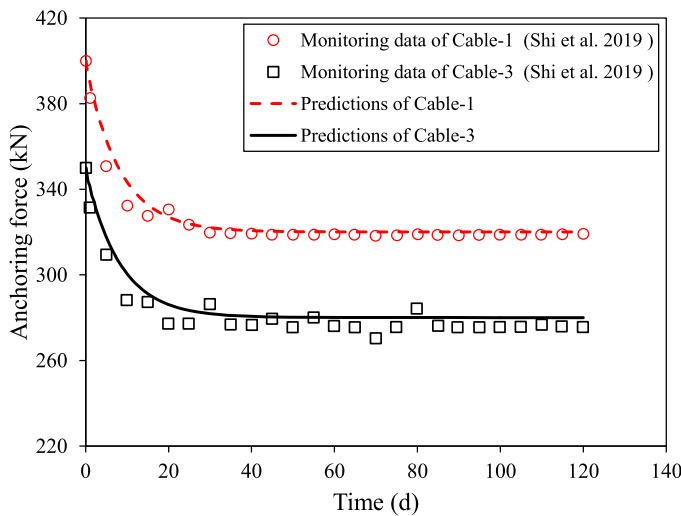
5. Applications to reported case examples

5.1. In situ monitoring tests for prestressed anchor cables

Shi et al. (2019) carried out an in situ monitoring test for prestressed anchor cables in a deep cutting slope. The rock mass of the slope was mainly quartz schist. The cable was 22 m in total length, 12 m in free segment, 10 m in anchorage segment, and 130 mm in anchor hole diameter. Each anchor cable consisted of four steel strands. The diameter of each steel strand was 15 mm, the tensile strength was 1860 MPa, and the elastic modulus was 195 GPa. The cement mortar was used in grouting with water cement ratio of 1:1. E of the anchoring body was calculated as 30 GPa. Monitoring test results of cables 1 and 3 were predicted. The designed pretensions were 400 and 350 kN for the two cables, respectively, and the monitoring time was 120 days. Merchant model parameters were determined by fitting analysis: $G_0 = 2.5$ MPa,

Fig. 12. Comparisons between the analytical predictions proposed in this paper and in situ monitoring data from Shi et al. 2019. [Color online.]

Fig. 13. Comparisons between the analytical predictions proposed in this paper and physical model testing results (physical model tests conducted by Chen et al. 2002). [Color online.]
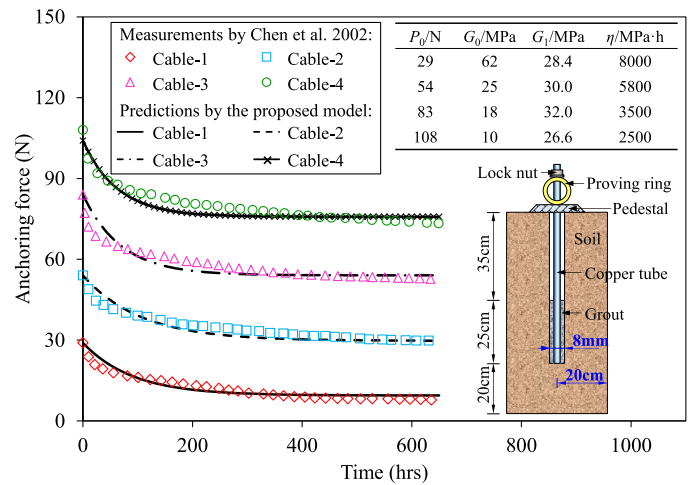

Fig. 14. Loss rate of anchoring force α versus bond length L_a with various G_1/G_0. [Color online.]

$G_1 = 5.2$ MPa, and $\eta = 55$ MPa·d. Figure 12 illustrates the good matches between the analytical predictions proposed in this paper and the monitoring data.

5.2. Physical model test for prestressed anchors embedded in soft rock

Chen et al. (2002) conducted four groups of pullout physical model tests aimed at studying the anchoring force loss behavior of prestressed anchors. The anchors are 60 cm in total length, 35 cm in free length, 25 cm in bond length, and 8 mm in anchor hole diameter. Yellow sticky sand was used to simulate soft rock. The anchor body was a copper tube with a diameter of 6 mm and thickness of 2 mm. The tensile strength of the copper tube was 1080 N, and the elastic modulus was 132 GPa. The grouting used 425# cement. The E of the anchoring body was calculated as 75 GPa. The designed pretensions were 29, 54, 83, and 108 N for the four model anchors, and the testing time was 650 h. Model parameters were calculated by fitting the experimental data. Figure 13 illustrates comparisons between theoretical predictions proposed in this paper and the tests results. Both the in situ monitoring data and model test results are in good agreement with the theoretical calculations, which proves that the proposed theoretical modeling framework is effective for predicting the anchoring force loss behaviors of prestressed ground anchors.

6. Parametric studies

Taking the element-scale pullout stress relaxation test ($\tau_0 = 40$ kPa) as the baseline, the presented theoretical modeling framework was used to investigate the impacts of model parameters on the derived anchoring force loss response. The parameters of interest in this parametric analysis comprised the interface shear modulus ratio G_1/G_0, bond length L_a, free length L_f, and axial stiffness of the free segment E_bA_b.
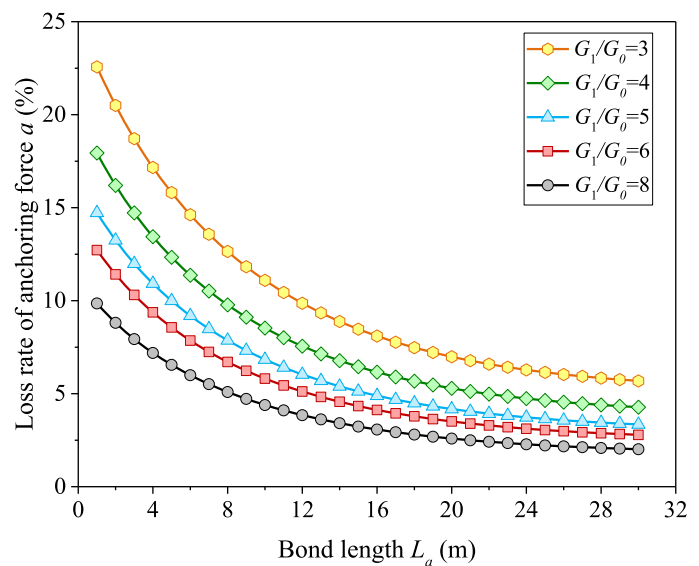
6.1. Effect of the interface shear modulus ratio G_1/G_0

As an empirical fact, the soil strength can be reflected by G_1/G_0. Specifically, smaller soil strength generally results in greater rheological deformation and a smaller magnitude of G_1/G_0. The loss rate of the anchoring force α versus the bond length L_a with various G_1/G_0 is plotted in Fig. 14. The calculations demonstrate that a smaller G_1/G_0 leads to a greater α. In addition, α is found to decrease with increasing L_a. Hence, compared with pan soil, prestressed anchors embedded in soft soil may need a longer bond length to resist anchoring force loss. However, the decreasing magnitude of α is very small once the bond length exceeds a critical value, which indicates that increasing the bond length is not a good choice for reducing anchoring force loss in practice.

Fig. 15. Loss rate of anchoring force α versus free length L_f with various bond lengths L_a. [Color online.]

Fig. 16. Loss rate of anchoring force α versus axial stiffness of free segment $E_b A_b$ with various bond lengths L_a. [Color online.]
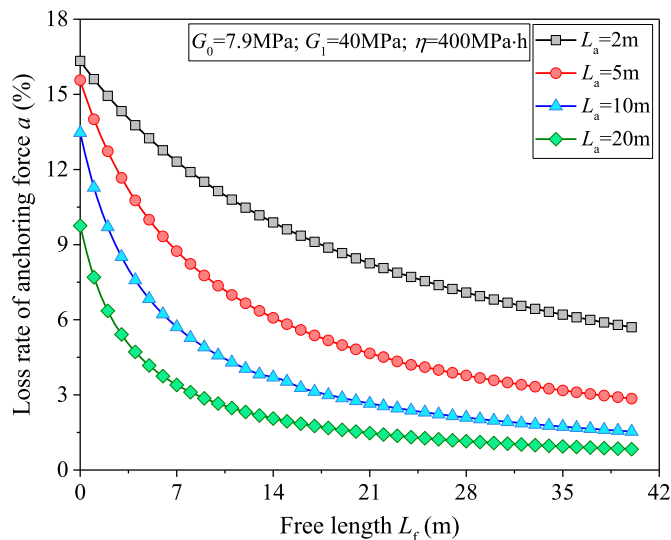
Hence, an appropriate value/range of anchoring force loss α is indeed important for effective functionality in design practice. The recommended range of α was 6%~8% when the soil was equipped with moderate strength (G_1/G_0 was 4~6 in this study). The recommended value/range of α would be smaller provided that the anchors were installed in pan soil/rocks, otherwise its recommendation would be larger.
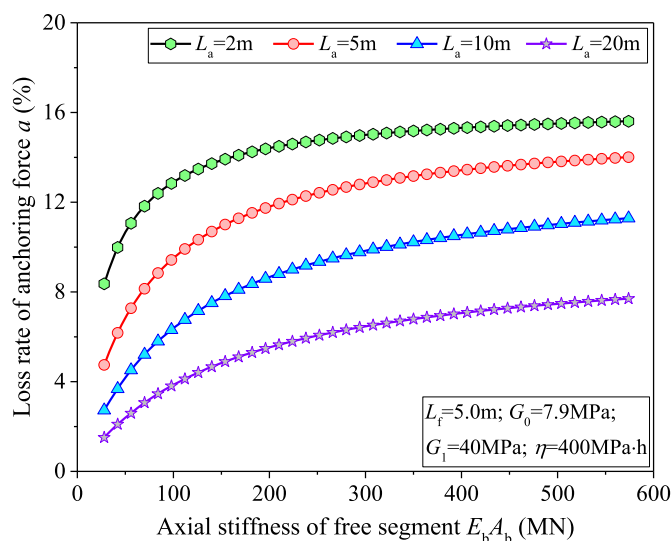
6.2. Effect of the free length L_f

The anchoring force loss is found to decrease with increasing L_f, but the magnitude of decrease is very small once L_f exceeds a critical value, as shown in Fig. 15. This phenomenon is due to the continuous development of the soil–grout interface shear stress as time elapses. Specifically, α continuously develops as time increases, leading to a decrease in the tensile deformation of the free segment δ_b. The displacement at the anchor head s_h is constant, so the pullout displacement s_0 increases, as calculated by eq. 10. Furthermore, the soil–grout interface shear stress increases persistently due to the increasing interface shear displacement. α gradually tends to stabilize in the dynamic process. In addition, a longer L_f will result in a greater reduction in δ_b, a greater increase in s_0, and a greater development of interface shear stress. Another merit of a long free segment is the diminishing of the impact of anchoring force loss caused by pedestal looseness. As stipulated in the Chinese technical specification CECS 22 (2005), the free length for prestressed anchors should not be less than 5.0 m. Nonetheless, it is not advisable to reduce the anchoring force loss by excessively increasing the free length due to the low efficiency.

6.3. Effect of the axial stiffness of the free segment $E_b A_b$

Figure 16 shows that a greater $E_b A_b$ leads to greater anchoring force loss, which is related to the tensile deformation of the free segment δ_b. Specifically, a greater $E_b A_b$ leads to a smaller decrease of δ_b and an equal smaller increment of s_0, which limits the development of interface shear stress. Therefore, on the premise of meeting the tensile strength of the free segment, it will be an excellent choice to reduce its axial stiffness in design practice, for instance, cutting down the amount of steel strand/rebar, using structural materials with a smaller elasticity modulus. Steel strands and ribbed steel rebar are most widely used in anchoring engineering. Their moduli are similar, but the tensile strength of a steel strand is much greater than that of rebar. Much less steel strand is needed to meet the strength demand, so the corresponding axial stiffness is much smaller. Hence, compared with steel rebar, it may be more suitable to use steel strands for prestressed anchors in practice.

7. Importance and practical application of this study

The practical application of the developed theoretical modeling framework is that once the interface parameters are obtained from long-term element-scale pullout tests, it can be subsequently used to predict the time-dependent mechanical behavior for prestressed ground anchors. Specifically, (*i*) calculate the anchoring force loss for prestressed anchors in their service period; (*ii*) assess whether re-tensioning is needed for prestressed anchors provided that the locking load or the allowable anchoring force loss is designed; (*iii*) predict the time for re-tensioning if the process is necessary, etc. Moreover, some research findings can be utilized to determine some more suitable anchor materials and analyze the mechanical mechanism of some phenomena, such as the length effect of the free segment. Overall, the findings achieved in this study are expected to facilitate the design practice process regarding the long-term performance of prestressed anchor engineering.

The research findings were applied to design practice. Monitoring tests conducted by Shi et al. (2019) were taken as the typical example. It was assumed that the locking load of cable 1 was 300 kN. The cable with pretension of 400 kN in the original design can meet the bearing capacity requirement. Ulteriorly, the pretension is now redesigned as 370 kN. Based on the predictions, the anchoring force will decrease to the locking load of 300 kN on day 27, which means that the anchors need re-tensioning before that day. The anchoring force will decrease to the locking load on day 7 if the pretension is designed as 350 kN. Additionally, increasing the free length L_f, bond length L_a, or anchor hole diameter D can also reduce the anchoring force loss. For instance, α would be reduced by approximately 2% provided that L_f could increase by 3.0 m.

8. Limitations

In this study, the Merchant rheological model was adopted to characterize the interaction between the grout and surrounding soil. Tertiary creep cannot be simulated by this model. Additionally, the tension rod and cement grout were all assumed to be elastic. The assumption should be improved provided that some materials characterized by significant rheological behaviors are used, such as fiber-reinforced polymer materials or resin materials (Zhang et al. 2001, 2015; Yang et al. 2014; Fan et al. 2017). Therefore, the coupled interactions among the complicated interface rheology and material rheology can be considered, which is indeed a more accurate modeling, but it will also bring new and incredible challenges.

9. Conclusions

Theoretical and experimental investigations of anchoring force loss behavior for prestressed ground anchors were conducted in this paper. The following main conclusions can be drawn from the results:

1. A theoretical modeling framework was developed to predict the time-dependent mechanical responses of prestressed ground anchors, in particular the anchoring force loss and evolution of load-transfer responses over time. The reasonable matches between the theoretical calculations and measurements in in situ loading tests and model tests verified the applicability and effectiveness of the theoretical modeling framework.
2. An element-scale pullout stress relaxation test and a large-scale model test of pretension loading were performed on a prestressed anchor. A significant relaxation over the grout–laterite interface was found in the tests, indicating the importance of considering the interface's rheological behavior in the theoretical modeling for prestressed ground anchors.
3. The element-scale pullout stress relaxation test can be effectively applied to characterize the soil–grout interface relaxation behavior by calibrating the Merchant model parameters, provided that the material properties and testing conditions of the element-scale anchor specimen are representative of those of anchors in the field.

4. Prestressed anchors with a smaller G_1/G_0, smaller free length L_f, and greater axial stiffness $E_b A_b$ tend to exhibit greater anchoring force loss. Compared with pan soil, prestressed anchors embedded in soft soil may need longer bond length L_a and free length L_f to resist anchoring force loss. However, excessively increasing the bond length or free length is not advisable due to the low efficiency.

List of symbols

A	cross-sectional area of anchorage segment
A_b	cross-sectional area of tension rod
A_g	cross-sectional area of grout
d	diameter of grout
E	Young's modulus of anchorage segment
E_b	elasticity modulus of tension rod
E_g	elasticity modulus of grout
G_0	soil–grout interface shear modulus
G_1	soil–grout interface shear modulus
L_a	bond length
L_f	free length
n	number of anchor units
P_0	designed pre-tension (initial anchoring force)
$P(x, t)$	tensile force of the anchor
s_h	constant pullout displacement at anchor head
$s(x, t)$	axial pullout displacement
t	time
t_0	initial time
t_1	$t_0 + \Delta t$
Δt	calculation step of time
x	distance from the tensioned end
x_i	location of the ith node
Δx	L_a/n
α	loss rate of anchoring force
$\delta_b(t)$	tensile deformation of tension rod in free segment
$\varepsilon(x, t)$	axial strain of grouted anchor
η	soil–grout interface shear viscosity coefficient
μ_p	perimeter of anchor
τ_0	interface shear stress at the initial moment
$\tau(x, t)$	soil–grout interface shear stress

Article information

Copyright

Author information

Author ORCIDs

Shimin Zhu https://orcid.org/0000-0002-7464-8227
Changfu Chen https://orcid.org/0000-0002-4800-5615

References

Benmokrane, B., and Balllivy, G. 1991. Five-year monitoring of load losses on prestressed cement-grouted rock anchors. Canadian Geotechnical Journal, **28**: 668–677. doi: 10.1139/t91-081.

Benmokrane, B., Chennouf, A., and Mitri, H.S. 1995. Laboratory evaluation of cement-based grouts and grouted rock anchors. International Journal of Rock Mechanics and Mining Sciences & Geomechanics Abstracts, **32**(7): 633–642. doi:10.1016/0148-9062(95)00021-8.

Brown, E.T. 2015. Rock engineering design of post-tensioned anchors for dams—a review. Journal of Rock Mechanics and Geotechnical Engineering, **7**(1): 1–13. doi: 10.1016/j.jrmge.2014.08.001.

Bryson, L.S., and Giraldo, J.R. 2020. Analysis of case study presenting ground anchor load-transfer response in shale stratum. Canadian Geotechnical Journal, **57**: 85–99. doi:10.1139/cgj-2018-0326.

CECS 22. 2005. Technical specification for ground anchors. China Planning Press, Beijing, China.

Chen, A.M., Gu, J.C., Shen, J., and Ming, Z.Q. 2002. Model testing research on the variation of tension force of anchor cable with time in reinforcement of soft rocks. Chinese Journal of Rock Mechanics and Engineering, **21**(2): 251–256. doi: 10.3321/j.issn:1000-6915.2002.02.020.

Chen, C.F., Liang, G.T., Tang, Y., and Xu, Y.L. 2015. Anchoring solid–soil interface behavior using a novel laboratory testing technique. Chinese Journal of Geotechnical Engineering, **37**(6): 1115–1122. doi:10.11779/CJGE201506018.

Chen, C.F., Liu, J.B., Xu, Y.L., and Zhang, G.B. 2016. Tests on shearing creep of anchor–soil interface and its empirical model. Chinese Journal of Geotechnical Engineering, **38**(10): 1762–1768. doi: 10.11779/CJGE201610003.

Chen, C.F., Zhu, S.M., Zhang, G.B., Mao, F.S., and Cai, H. 2021. Time-dependent load transfer behavior of grouted anchors in laterite. Computers and Geotechnics, **132**: 103969. doi: 10.1016/j.compgeo.2020.103969.

Chen, G.Q., Chen, T., Chen, Y., Huang, R.Q., and Liu, M. 2018. A new method of predicting the prestress variations in anchored cables with excavation unloading destruction. Engineering Geology, **241**: 109–120. doi: 10.1016/j.enggeo.2018.05.015.

Chen, J.H., Hagan, P.C., and Saydam, S. 2017. Sample diameter effect on bonding capacity of fully grouted cable bolts. Tunnelling and Underground Space Technology, **68**: 238–243. doi: 10.1016/j.tust.2017.06.004.

Chu, L.M., and Yin, J.H. 2005. Comparison of interface shear strength of soil nails measured by both direct shear box tests and pullout tests. Journal of Geotechnical and Geoenvironmental Engineering, **131**: 1097–1107. doi: 10.1061/(ASCE)1090-0241(2005)131:9(1097).

Cooke, R.W., Price, G., and Tarr, K. 1979. Jacked piles in London Clay: a study of load transfer and settlement under working conditions. Géotechnique, **29**(2):113–147. doi: 10.1680/geot.1979.29.2.113.

Ehrlich, M., and Silva, R.C. 2015. Behavior of a 31 m high excavation supported by anchoring and nailing in residual soil of gneiss. Engineering Geology, **191**: 48–60. doi: 10.1016/j.enggeo.2015.01.028

Fan, H.F., Vassilopoulos, A.P., and Keller, T. 2017. Pull-out behavior of CFRP single-strap ground anchors. Journal of Composites for Construction, **21**(3): 4016102. doi: 10.1061/(ASCE)CC.1943-5614.0000760

Fang, H.Y. 1991. Foundation engineering handbook. 2nd ed. Chapman & Hall, New York, NY.

Farmer, I.W. 1975. Stress distribution along a resin grouted rock anchor. International Journal of Rock Mechanics and Mining Sciences & Geomechanics Abstracts, **12**: 347–351. doi: 10.1016/0148-9062(75)90168-0.

Hobst, L., and Zajic, J. 1983. Anchoring in rock and soil. 2nd ed. Elsevier Scientific Publishing, Amsterdam.

Hong, C.Y., Yin, J.H., Zhou, W.H., and Pei, H.F. 2012. Analytical study on progressive pullout behavior of a soil nail. Journal of Geotechnical and Geoenvironmental Engineering, **138**(4): 500–507. doi: 10.1061/(ASCE)GT.1943-5606.0000610.

Kim, N.K. 2003. Performance of tension and compression anchors in weathered soil. Journal of Geotechnical and Geoenvironmental Engineering, **129**(12): 1138–1150. doi: 10.1061/(ASCE)1090-0241(2003)129:12(1138).

Li, C.C. 2017. Rockbolting: pinciples and aplications. Butterworth-Heinemann, Oxford, UK.

Ma, S.Q., Nemcik, J., and Aziz, N. 2013. An analytical model of fully grouted rock bolts subjected to tensile load. Construction and Building Materials, **49**: 519–526. doi: 10.1016/j.conbuildmat.2013.08.084.

Martín, L.B., Tijani, M., and Hadj-Hassen, F. 2011. A new analytical solution to the mechanical behaviour of fully grouted rockanchors subjected to pull-out tests. Construction and Building Materials, **25**(2): 749–755. doi: 10.1016/j.conbuildmat.2010.07.011.

Ozhan, H.O., and Guler, E. 2018. Critical tendon bond length for prestressed ground anchors in pullout performance tests conducted in sand. International Journal of Civil Engineering **16**: 1329–1340. doi: 10.1007/s40999-017-0261-0.

Rajaie, H. 1990. Experimental and numerical investigations of cable bolt support systems. Ph.D. thesis, McGill University, Montreal, QC.

Shi, K.Y., Wu, X.P., Liu, Z., and Dai, S.L. 2019.Coupled calculation model for anchoring force loss in a slope reinforced by a frame beam and anchor cables. Engineering Geology, **260**: 105245. doi: 10.1016/j.enggeo.2019.105245.

Štefaňák, J., Miča, L., Chalmovský, J., Leiter, A., and Tichý, P. 2017. Full-scale testing of ground anchors in neogene clay. Procedia Engineering, **172**: 1129–1136. doi: 10.1016/j.proeng.2017.02.170.

Tan, T.K., and Kang, W.F. 1980. Locked in stresses, creep and dilatancy of rocks, and constitutive equations. Rock Mechanics, **13**(1): 5–22. doi:10.1007/BF01257895.

Yang, M.J., Zhao, Y.M., and Zhang, N. 2014. Creep behavior of epoxy-bonded anchor system. International Journal of Rock Mechanics and Mining Sciences, **67**: 96–103. doi: 10.1016/j.ijrmms.2014.02.001.

Zhang, B., and Benmokrane, B. 2005. Large model test of prestressed carbon fibre reinforced polymer ground anchors. Canadian Journal of Civil Engineering, **32**: 1064–1074. doi:10.1139/l05-058.

Zhang, B., Benmokrane, B., Chennouf, A., Mukhopadhyaya, P., and El-Safty, A. 2001. Tensile behavior of FRP tendons for prestressed ground anchors. Journal of Composites for Construction, **5**(2): 85–93. doi: 10.1061/(ASCE)1090-0268(2001)5:2(85).

Zhang, C.C., Zhu, H.H., Xu, Q., Shi, B., and Mei, G.X. 2015. Time-dependent pullout behavior of glass fiber reinforced polymer (GFRP) soil nail in sand. Canadian Geotechnical Journal, **52**: 671–681. doi: 10.1139/cgj-2013-0381.

Zhang, G.B., Chen, C.F., Zornberg, J.G., Morsy, A.M., and Mao, F.S. 2020. Interface creep behavior of grouted anchors in clayey soils: effect of soil moisture condition. Acta Geotechnica, **15**: 2159–2177. doi: 10.1007/s11440-019-00907-6.

Zhu, S.M., Chen, C.F., Mao, F.S., and Cai, H. 2021. Application of disturbed state concept for load-transfer modeling of recoverable anchors in layer soils. Computers and Geotechnics, **137**: 104292. doi: 10.1016/j.compgeo.2021.104292.

1600

Can. Geotech. J. **59**: 1587–1601 (2022) | dx.doi.org/10.1139/cgj-2021-0220

Appendix A. Derivation of the boundary value conditions

At the moment $t = 0$ (t_0), eq. 6 can be rewritten as

(A1) $\tau(x, t_0) = G_0 s(x, t_0)$

Combining eqs. 1, 2, and 5 with eq. A1 , eq. 7 can be deduced as

(A2) $\dfrac{d^2 s(x, t_0)}{dx^2} - \dfrac{\mu_p G_0}{EA} s(x, t_0) = 0$

The analytical solution of eq. A2 can be expressed as

(A3) $s(x, t_0) = C_1 e^{\beta x} + C_2 e^{-\beta x}$

where $\beta = \sqrt{\mu_p G_0 / EA}$; C_1 and C_2 are undetermined parameters.

The distributions of tensile force and shear stress over bond length are calculated by substituting eq. A3 into eq. 17 and eq. 21, respectively.

(A4) $P(x, t_0) = \beta EA \left(C_2 e^{-\beta x} - C_1 e^{\beta x} \right)$

(A5) $\tau(x, t_0) = G_0 \left(C_2 e^{-\beta x} - C_1 e^{\beta x} \right)$

Parameters C_1 and C_2 are determined using eq. 10:

(A6) $\begin{cases} C_1 = \dfrac{s_0}{(e^{2\beta L_a} + 1)} \\ C_2 = \dfrac{s_0 e^{2\beta L_a}}{(e^{2\beta L_a} + 1)} \end{cases}$

The relationship between P_0 and s_0 can be deduced by eqs. A3 and A5:

(A7) $P(x_0, t_0) = P_0 = \dfrac{\beta EA s_0}{(e^{2\beta L_a} + 1)} \left(e^{2\beta L_a} - 1 \right)$

Further, eq. A7 can be rewritten as

(A8) $s_0 = \dfrac{P_0 \left(e^{2\beta L_a} + 1 \right)}{\beta EA \left(e^{2\beta L_a} - 1 \right)}$

The initial conditions of eq. 7 can be obtained by substituting eqs. A6 and A8 into eqs. A3–A5, which is shown in eq. 9. Additionally, the constant pullout displacement at the anchor head s_h corresponding to P_0 is deduced as

(A9) $s_h = s_0(x_0, t_0) + \delta_b(t_0) = P_0 \left[\dfrac{\left(e^{2\beta L_a} + 1 \right)}{\beta EA \left(e^{2\beta L_a} - 1 \right)} + \dfrac{L_f}{E_b A_b} \right]$